

Neural network potentials for dynamics and thermodynamics of gold nanoparticles

Cite as: J. Chem. Phys. **146**, 084314 (2017); <https://doi.org/10.1063/1.4977050>

Submitted: 17 December 2016 . Accepted: 08 February 2017 . Published Online: 28 February 2017

Siva Chiriki, Shweta Jindal, and Satya S. Bulusu



View Online



Export Citation



CrossMark

ARTICLES YOU MAY BE INTERESTED IN

[Spherical harmonics based descriptor for neural network potentials: Structure and dynamics of Au₁₄₇ nanocluster](#)

The Journal of Chemical Physics **146**, 204301 (2017); <https://doi.org/10.1063/1.4983392>

[Perspective: Machine learning potentials for atomistic simulations](#)

The Journal of Chemical Physics **145**, 170901 (2016); <https://doi.org/10.1063/1.4966192>

[Atom-centered symmetry functions for constructing high-dimensional neural network potentials](#)

The Journal of Chemical Physics **134**, 074106 (2011); <https://doi.org/10.1063/1.3553717>

Lock-in Amplifiers
up to 600 MHz



Zurich
Instruments



Neural network potentials for dynamics and thermodynamics of gold nanoparticles

Siva Chiriki, Shweta Jindal, and Satya S. Bulusu^{a)}

Discipline of Chemistry, Indian Institute of Technology (IIT) Indore, Madhya Pradesh 453552, India

(Received 17 December 2016; accepted 8 February 2017; published online 28 February 2017)

For understanding the dynamical and thermodynamical properties of metal nanoparticles, one has to go beyond static and structural predictions of a nanoparticle. Accurate description of dynamical properties may be computationally intensive depending on the size of nanoparticle. Herein, we demonstrate the use of atomistic neural network potentials, obtained by fitting quantum mechanical data, for extensive molecular dynamics simulations of gold nanoparticles. The fitted potential was tested by performing global optimizations of size selected gold nanoparticles (Au_n , $17 \leq n \leq 58$). We performed molecular dynamics simulations in canonical (NVT) and microcanonical (NVE) ensembles on Au_{17} , Au_{34} , Au_{58} for a total simulation time of around 3 ns for each nanoparticle. Our study based on both NVT and NVE ensembles indicate that there is a dynamical coexistence of solid-like and liquid-like phases near melting transition. We estimate the probability at finite temperatures for set of isomers lying below 0.5 eV from the global minimum structure. In the case of Au_{17} and Au_{58} , the properties can be estimated using global minimum structure at room temperature, while for Au_{34} , global minimum structure is not a dominant structure even at low temperatures. Published by AIP Publishing. [<http://dx.doi.org/10.1063/1.4977050>]

I. INTRODUCTION

Finite time and finite temperature properties of chemical systems are often obtained using Molecular Dynamics (MD) or Monte Carlo (MC) simulations. These simulations use classical interatomic potentials or *ab initio* methods to evaluate the energy and forces of the system. One has to compromise in accuracy for using classical potentials, which are usually computationally cheap. On the other hand, *ab initio* methods are very accurate in describing the structure and properties of chemical systems but often are computationally prohibitive as the system size increases. If the chemical system is a finite system, such as molecular or atomic nanoparticles, system's structure and properties are very much size dependent.^{1,2} Especially in the case of metal nanoparticles such as gold, interesting chemical and physical properties can be exploited for applications in chemistry and biology.^{3–5} Since the properties of nanoparticles and the structure are inter-related, it is always important to begin by identifying the structure of nanoparticle.

It is well known that gold nanoparticles have unusual structures primarily due to strong relativistic effects.^{6,7} The direct consequences of relativistic effects are contraction of 6s orbital and expansion of 5d orbital, reduced gap between 6s and 5d orbitals, and a strong s-d hybridization. Therefore, in pure gold nanoparticles we can expect some directionality in the bonding which is due to presence of d-orbital, unlike copper (or silver) nanoparticles which undergo only metallic bonding. That is why, small gold nanoparticles exhibit planar structures⁸ while medium-sized gold nanoparticles exhibit variety of structures including hollow cages^{9,10} and pyramids.¹¹

Therefore, to study finite systems such as gold nanoparticles at reasonable time scales (in ns) and at realistic temperatures (≥ 300 K), there is a necessity to obtain a method that can treat quantum effects (electronic effects, relativistic effects) as well as be computationally inexpensive. Enormous progress has been made to deal with the computational complexity by developing linear scaling methods such as Spanish Initiative for Electronic Simulations with Thousands of Atoms (SIESTA)¹² and Orbital Free Density Functional Theory (OFDFT) methods.¹³ In other approaches, artificial neural network (NN) based potentials,^{14,15} GAP potentials,¹⁶ GABEF potentials,¹⁷ and on-the-fly fittings¹⁸ were constructed to approximate the potential energy surfaces of bulk materials. Behler *et al.* reported artificial NN^{19–21} potentials to study a variety of bulk systems,^{22,23} multicomponent systems,^{24–27} and H_2O nanoparticles.²⁸ Further, this artificial NN was extended to study nanoparticles.^{26,27,29,30} and multicomponent oxide systems.^{31,32} Recently, a deep NN fitting global optimization technique was constructed to study small Pt nanoparticles.³³

In this paper, we used Behler's artificial NN approach³⁴ to construct an interaction potential by fitting density functional theory (DFT) data for Au_n nanoparticles, with $17 \leq n \leq 58$. We call this as atomistic Neural Network (ANN) potential. Similar technique was earlier used to study finite temperature properties of medium-sized Na nanoparticles³⁰ in which structures and melting properties obtained were identical to those obtained using high level *ab initio* methods. Born Oppenheimer MD simulations require extensive parallel computing and a huge amount of computational time to obtain equilibrium properties for medium sized Au nanoparticles. To our knowledge, few studies were reported on Au nanoparticles, in which Born Oppenheimer MD studies were carried out at

^{a)}sbulusu@iiti.ac.in

single temperature ($T = 300$ K) to study fluxional behaviour³⁵ and also to predict structures.³⁶

Using ANN, we first obtained the Global Minimum (GM) structures and low lying isomers for size selected Au_n nanoparticles. In the last decade many theoretical studies reported the global optimizations on small to medium sized Au nanoparticles using *ab initio* methods.^{11,37–41} Some of the studies include experimental and theoretical approaches to probe the structure of anionic Au nanoparticles.^{8,9,42–48} Enormous progress has been made on finite-size nanoparticles at finite temperatures.^{49–54} To understand the gold nanoparticles at finite temperatures, we have to calculate the probability of GM at finite temperature. For this, we adopted the procedure Li and Truhlar⁵⁵ to approximate the partition function, which consists of potential energy and vibrational (by considering harmonic-oscillator approximations) and rotational (by considering rigid rotor approximations) contributions, respectively, for all the isomers considered.

In nanoparticles, due to large surface to volume ratio, melting process is usually characterized by a broad peak in heat capacity curve, unlike a sharp peak in the bulk material. The broad peak is due to phase coexistence behaviour in nanoparticles, where there is dynamic coexistence of solid-like and liquid-like phases. The atomistic level explanation of dynamic phase coexistence has been an interesting topic theoretically and experimentally.^{49–51,56} Recently, gallium nanoparticles on sapphire substrate were shown to exhibit stable coexistence of liquid and solid phases experimentally.⁵⁷ Since the phase coexistence has a strong technological relevance, we intend to study the melting process of Au nanoparticles. Melting studies were conducted at two different statistical descriptions, constant temperature and constant energy, of the nanoparticle system to get a comprehensive understanding. We used caloric curves, heat capacities, and order parameters such as change in volume of the particles along trajectory to examine the melting process. Calculations of equilibrium constant for the phase coexistence by using the method proposed⁵⁸ by Englemann *et.al.* was adopted for quantifying the melting process.

In the present study, we consider three gold nanoparticles, Au_{17} , Au_{34} , and Au_{58} , to study the finite temperature and finite time properties. Au_{17} is the smallest known cage structure,⁹ which was considered to test the accuracy of ANN potential. Anionic Au_{34} is the first predicted^{35,43} fluxional core-surface structure, with a 4-atom core, an electronic surface closing, and a high band gap (0.94 eV). DFT calculations on Au_{34} ⁵⁹ also show its high affinity for CO and O₂, making it a good candidate for catalysis. In the case of Au_{58} , it was predicted that Au_{58} in its anionic form exhibits large band gap and a major surface closing.⁴⁷ It is a near spherical structure with C_1 point group symmetry. Core of Au_{58} is a symmetric 10 atom b-tetragonal square anti-prism (BSA) structure. It was predicted that such a low symmetry structure may contain many surface defects,⁴⁷ which can be responsible for strong catalytic activity and therefore understanding, the structural dynamics at the atomistic level become essential. To our knowledge, this is the first comprehensive finite temperature and finite time study on sub-nanometer gold nanoparticles, to get a fundamental understanding of the functioning of the nanoparticle at

an atomistic level. In this paper, we only focus on free standing gold nanoparticles.

In Sec. II, we provide details of ANN architecture and fitting procedure, and we describe, in detail, optimization of weight parameters required to train the ANN using adaptive global extended Kalman filter (AGEKF).^{60–62} In Sec. III, we focused on calculating MD trajectories using ANN potential to evaluate the physical properties such as melting transitions in NVE and NVT ensembles, evaluating equilibrium constant at phase coexistence region, and evaluating the probability of isomer at a given temperature to understand the fluxionality in the systems considered.

II. METHODOLOGY AND COMPUTATIONAL DETAILS

All the calculations are done using VASP package.⁶³ The Perdew, Burke, and Ernzerhof (PBE) functional has been used for treating exchange correlation of electrons at generalised gradient approximation (GGA) level of theory with plane wave basis set.⁶⁴ Projector Augmented Wave (PAW) method was used to treat valence electrons(5d¹⁰ 6s¹) explicitly with scalar relativistic effects and their interactions with core electrons.⁶⁵ Gamma k-point ($1 \times 1 \times 1$) mesh is used to sample the Brillouin zone. We have used $22 \times 22 \times 22$ box length for nanoparticles size $\leq \text{Au}_{20}$ and $25 \times 25 \times 25$ box length for sizes $\geq \text{Au}_{21}$ with a constant vacuum dimension of 12 Å. The energy cutoff is kept at 250.0 eV, and threshold for energy and forces are set as 1×10^{-4} and 1×10^{-3} , respectively. We refer the PBE functional along with plane wave basis set (including PAW method) as DFT elsewhere in the manuscript.

A. Initial data generation

To construct the preliminary ANN potential, we generated 3000 data points by using DFT MD simulations and by using MC simulations with Gupta many body potential^{66,67} at different temperatures, starting with different random geometries. The data contain nanoparticles of various sizes in the range of Au_{15} to Au_{60} . Similar types of isomers are removed by using the shape detecting algorithm. Preliminary ANN potential was used for generating more data using MD simulations.

B. Structure of feed-forward neural networks

A two layer feed-forward NN architecture was used to construct ANN potentials shown as follows:

$$E_i = \sum_{l=1}^{N_{hd}} W_{ll}^{23} \cdot f_l^2 \left[Wb_l^2 + \sum_{k=1}^{N_{hd}} W_{kl}^{12} \cdot f_k^1 \left(Wb_k^1 + \sum_{j=1}^{N_D} W_{jk}^{01} \cdot D_{ij} \right) \right], \quad (1)$$

where E_i is energy of i th atom and N_{hd} is number of hidden nodes. D_{ij} is input descriptor functions of length N_D for i th atom. W_{jk}^{01} , W_{kl}^{12} , and W_{ll}^{23} are weights connecting from the input layer to hidden layer one, hidden layer one to hidden layer two, and hidden layer two to output layer, respectively. Wb_l^2 and Wb_k^1 are bias weights in hidden layer one and hidden layer two, respectively. f_l^2 and f_k^1 represent the sigmoid function for activation of the network.

In the present study, we use 30 nodes in each hidden layer and 51 input functions. The network comprises 2520 weights(N_w). The total energy (E) of a nanoparticle is computed by summing all the atomic energies,

$$E = \sum_i E_i. \quad (2)$$

C. Local atomic environment descriptors

To describe the local atomic environment around each atom, we used Behler-Parrinello functions,²⁰ which are the radial and angular functions shown in Equations (3) and (4), respectively,

$$D_i^{rad} = \sum_{i \neq j} e^{-\eta R_{ij}^2} f_c(R_{ij}), \quad (3)$$

$$D_i^{ang} = 2^{1-\zeta} \sum_{j,k \neq i} (1 + \lambda \cos \theta_{ijk})^\zeta e^{-\eta (R_{ij}^2 + R_{ik}^2 + R_{jk}^2)} \\ \times f_c(R_{ij}) \cdot f_c(R_{ik}) \cdot f_c(R_{jk}) \quad (4)$$

$$\cos \theta_{ijk} = \left[\frac{R_{ij} \cdot R_{ik}}{r_{ij} \cdot r_{ik}} \right], \quad (5)$$

where cosine cutoff function $f_c(R_{ij})$ is used with a cutoff radius of $R_c = 8.0 \text{ \AA}$. The cutoff function is defined as

$$f_c(R_{ij}) = \begin{cases} 0.5 \left[\cos \left(\frac{\pi R_{ij}}{R_c} \right) + 1 \right] & \text{if } R_{ij} \leq R_c, \\ 0 & \text{if } R_{ij} \geq R_c. \end{cases}$$

The input matrix D_{ij} is prepared by considering 9 radial functions and 42 angular functions for each atom with a set of parameters η, ζ, λ . All these parameters are provided in the supplementary material.

D. Scaling of input values

The inputs evaluated using radial and angular descriptors may be of large magnitudes. When we multiply these large numbers with weights, the final summation in Equation (1) becomes very large and sigmoid of large value will lead to saturation of node in feed forward NN. Hence, scaling is necessary to make all the input values to be present in some particular range. In the present study we used Behler's description²⁰ for scaling of descriptors. All input values are scaled between 0 and 1.

E. Analytical force calculation

ANN potential is a local atomic environment dependent potential. Hence, to represent an atom in a phase space correctly, we have to fit $3N$ force components in addition to one energy component. Therefore, the analytical force of k th atom in the direction $\alpha_{x,y,z}$ is given by the negative gradient of total energy of the nanoparticle, which is a summation of the product of derivative of the network function ($\frac{\partial E}{\partial D}$) and derivative of descriptor functions ($\frac{\partial D}{\partial R_{k,\alpha}}$),

$$F_{k,\alpha} = -\frac{\partial E}{\partial R_{k,\alpha}} = -\sum_{i=1}^N \frac{\partial E_i}{\partial R_{k,\alpha}} = -\sum_{i=1}^N \sum_{j=1}^{M_s} \frac{\partial E_i}{\partial D_{i,j}} \frac{\partial D_{i,j}}{\partial R_{k,\alpha}}. \quad (6)$$

The expanded form of $F_{k,\alpha}$ is provided in the supplementary material.

F. Preparation of training data

The total set containing 12 000 data points is shuffled and divided into small binary files containing 300 data points each. The memory issues are avoided during the training process by using these binary files. The training is performed using 80% of data points, and 20% is utilised for testing.

G. Training of feed-forward neural networks

We implement AGEKF^{60–62} to optimize the weight parameters, which is a well-known technique and is very robust. The details of the technique, when used for optimization of weights obtained from ANN, are not much discussed in the literature. Here, we intend to provide qualitative details of the extended Kalman filter algorithm so that our results can be reproduced by others. The Kalman filter or linear quadratic estimator is an iterative method that uses a set of mathematical equations and consecutive data inputs to estimate an unknown quantity. In the case of ANN, we are interested in estimating weights of the network. Extended Kalman filter is a nonlinear version of original Kalman filter and is appropriate for estimating weight parameters in ANN because the NN output shown in Equation (1), i.e., the potential energy of i -th atom, is a nonlinear function of coordinates and weight parameters,

$$\hat{W}_{new} = \hat{W}_{old} + (K_G \times \hat{G}_E). \quad (7)$$

We begin from Equation (7), which tell us about the weight estimation in AGEKF. To estimate new weights (\hat{W}_{new}) from the old weights (\hat{W}_{old}), we require to know about Kalman gain (K_G) matrix and the difference between the reference value (measured value) and estimated value evaluated using old weights, i.e., the error vector \hat{G}_E ,

$$\hat{G}_E = [\hat{V}(x) - \hat{V}(x, \hat{W})], \quad (8)$$

$$\hat{V}(x) = [E^{DFT}, F_{\alpha_1}^{DFT}, F_{\alpha_2}^{DFT}, \dots, F_{\alpha_{3N}}^{DFT}], \quad (9)$$

$$\hat{V}(x, \hat{W}) = [E^{NN}, F_{\alpha_1}^{NN}, F_{\alpha_2}^{NN}, \dots, F_{\alpha_{3N}}^{NN}], \quad (10)$$

where $\hat{V}(x)$ and $\hat{V}(x, \hat{W})$ are $3N + 1$ component vectors containing one energy component and $3N$ force components of a data point for DFT and ANN. E^{DFT} and $F_{\alpha_{3N}}^{DFT}$ are DFT energy and forces whereas, E^{NN} and $F_{\alpha_{3N}}^{NN}$ are ANN energy and forces. Initially, weight parameters are randomly generated between 0 and 1. Using random initial weights, we evaluate ANN energy and the forces acting on an atom using Equations (1) and (6), respectively, for a given data point. Therefore, error vector comprises one energy component ($E_{DFT} - E_{NN}$) and $3N$ force components.

To avoid the trapping of weights in a local minima, a forgetting function is used,

$$\lambda_{new} = \lambda_0 \cdot \lambda_{old} + (1 - \lambda_0), \quad (11)$$

where λ_{new} is the time-varying forgetting factor. λ_0 and λ_{old} are initialized as 0.999 and 0.97, respectively,

$$K_G = \lambda_{new}^{-1} \left[\frac{P_{old} \cdot H^T}{\lambda_{new}^{-1} (H \cdot P_{old} \cdot H^T) + R} \right], \quad (12)$$

where $H = \frac{\partial \hat{V}(x, W)}{\partial W}$ is a derivative of energy and force network functions with respect to each weight. Therefore, H is a matrix of dimension $N_w \times 3N + 1$. K_G decides the estimation of new weights based on the relative magnitudes of error covariance matrix (P_{old}), and uncertainty in reference data (R). In Equation (12), if R is small, the new weight estimate depends mostly on the reference data and if $HP_{old}H^T$ is small compared to R , then the new weight estimate ignore the reference data and only rely on the older weights. In the latter case we can assume a converged solution for optimization of weights. For a reference data point, which is DFT energy and forces, it can be assumed that there is no numerical uncertainty in the data as the convergence criterion is kept same for all the data points in the DFT calculations. To achieve a smooth convergence in weight optimization, we add a measurement noise in the calculation of Kalman gain in Equation (12),

$$P_{new} = \lambda_{new}^{-1} [(I - K_G \cdot H) P_{old}] + Q, \quad (13)$$

where Q is a noise process covariance matrix and we initialised as a diagonal matrix with a constant value of 1×10^{-6} . We have to add the noise (Q) for updating the error covariance matrix to avoid exact state estimation. For updating the weights in each step, the Kalman filter uses the error covariance matrix of weights, P_{new} , which contains the information of direction of previous updates of weights. The P matrix is initialized as an identity matrix (I). The error covariance matrix gets updated at every step by using Equation (13). From Equation (13) we can conclude that if K_G is small, then a large value ($I - K_G$) gets multiplied to the old covariance matrix P_{old} and the P_{new} matrix is very close to the P_{old} matrix. From Equation (12), error in estimation is smaller compared to the small uncertainty, R , of the reference value. Therefore, if K_G is small, estimation of new weights relies mostly on the old weights ignoring any new reference data.

Here we will provide information about AGEKF stepwise:

- (1) First, we evaluate the total energy (E) and $3N$ force components of first reference point in data set with initial random weights, and then we calculate the error vector \hat{G}_E .
- (2) To linearize the neural network at each node, we have to determine the derivative of Equations (1) and (6) with respect to each weight, i.e., H matrix ($(3N + 1) \times N_w$).
- (3) Calculate the K_G matrix ($N_w \times (3N + 1)$) by using H matrix ($(3N + 1) \times N_w$) and initial P matrix ($N_w \times N_w$).

- (4) The weight vector is updated using Equation (7).
- (5) The error covariance matrix is updated using Equation (13)
- (6) Using updated weight vector, energy and forces of the second reference point are calculated. Similarly, weights are updated for all the reference points in an iteration.

H. Testing of trained ANN potentials

The training process is done iteratively and after every iteration, validation of the trained weights is done by calculating the average root mean square error (RMSE) of energy and forces. The equations for calculating RMSE are provided in the [supplementary material](#). After 76th iteration the average RMSE of testing started increasing, so the training process was stopped. The difference between average RMSE of training and testing, on an average, was 0.06 meV/atom for energy and 0.07 meV/Å for forces, as shown in Figure 1(a). The average RMSE of energy was 9 meV/atom and average RMSE of force was 88 meV/Å for the testing data set. The correlation plot between DFT energies (E_{DFT}) and ANN energies (E_{NN}) of test set is shown in Figure 1(b). It is evident from the correlation coefficient ($R^2 = 0.99$) that the accuracy of our ANN potential is comparable to that of DFT.

I. Computational time for energy calculation at ANN and DFT level

The time (in s) to compute energy and forces using ANN and DFT for nanoparticles of different sizes are tabulated in Table I. The DFT calculations are done in 16 cores CPU [GenuineIntel 2600.0 MHz], and ANN calculations are done in a single core CPU [GenuineIntel 2600.0 MHz]. Using ANN, the time for computing energy of a nanoparticle is of the order $N^{0.4}$, where N is the number of atoms in a nanoparticle and in the case of DFT it is around N^2 . Using ANN, we also calculated the time at every individual step for one complete calculation of energy and $3N$ components of forces of 147 atom nanoparticles as shown in Table II. From Table II, it is observed that 80% of total time is taken for the calculation of derivative of angular function, the equations for which are provided in the [supplementary material](#). This is because, in the case of angular functions we have to compute three body exponential functions and the derivative of angular functions involves matrices of dimensions $N \times N \times N$.

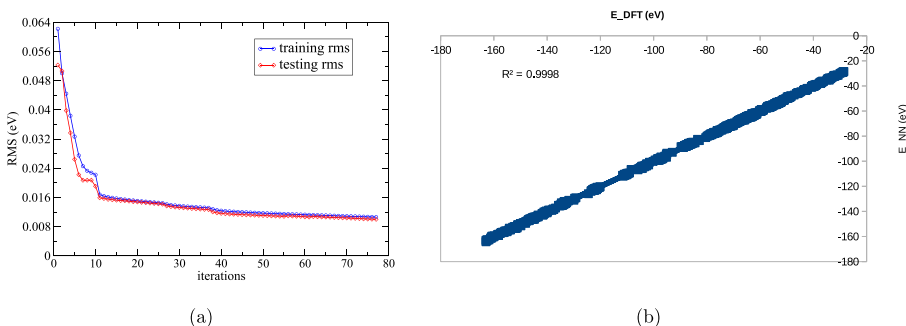


FIG. 1. (a) Training and testing decay, (b) correlation plot of DFT and NN energies.

TABLE I. Computational time for energy and forces at ANN and DFT level.

| Nanoparticles size | ANN time (s) | DFT time (s) |
|--------------------|--------------|--------------|
| 17 | 0.024 | 116 |
| 34 | 0.35 | 501 |
| 58 | 0.9 | 2 212 |
| 100 | 4.30 | 9 016 |
| 120 | 7.4 | 21 156 |
| 147 | 13.50 | 28 800 |

TABLE II. Computational time to compute energy and forces for Au_{147} at ANN.

| Number of atoms | D^{rad} (s) | D^{ang} (s) | $\frac{\partial D^{\text{rad}}}{\partial \alpha}$ (s) | $\frac{\partial D^{\text{ang}}}{\partial \alpha}$ (s) | E and F_{α} (s) |
|-----------------|-------------------------|-------------------------|--|--|-----------------------------|
| 147 | 0.08 | 1.497 | 0.007 | 10.91 | 1.38 |

III. RESULTS AND DISCUSSION

A. GM search of Au_n nanoparticles

For testing the accuracy of our potential, we performed the GM search on size-selected Au nanoparticles. For the GM search, we used basin hopping (BH) method⁶⁸ and also systematically quenched structures on multiple MD trajectories obtained at various temperatures ($T = 350$ K and $T = 700$ K). The structures which are less than 0.5 eV in energy from GM are considered for comparison using DFT. The collected structures and their relative energies are also compared with previous studies. All the low lying isomers for Au_{17} , Au_{34} , and Au_{58} are shown in Figure 2.

In the case of Au_{17} , ANN potential predicts two types of families, hollow cages (I,II,III,V) and pyramidal structures (IV,VI), as shown in Figure 2(a). Top 6 low lying structures were re-optimized using DFT. Hollow cage structure (I), with C_{2v} symmetry, is GM at both ANN and DFT levels. The pyramidal family structure (IV) is 0.08 eV high in energy with ANN potential and 0.21 eV with DFT from GM. In previous studies,⁶⁹ at PBE/DNP and PBEPBE/LANL2DZ level of theories, the hollow cage is still GM,⁶⁹ while the pyramidal family structures are 0.03 eV and 0.15 eV higher in energy relative to GM. Hence, ANN is consistent with respect to structures and their relative energies that are calculated using the above listed DFT functionals and basis sets.

In one of the studies,⁷⁰ using B3PW91/LANL2DZ level, the pyramidal structure is predicted as GM and the hollow cage structure is 0.01 eV high in energy compared to pyramidal structure. Another recent study⁷¹ at TPSS/def2-TZVP level structure predicted a structure that belongs to the pyramidal family with D_{2d} symmetry as GM. This structure is 0.18 eV lower in energy compared to the hollow cage structure. Therefore it should be noted that the GM structure and the relative energy magnitudes of low lying isomers will depend on the functional and type of basis set used. It is also evident that all the above functionals have predicted both pyramidal and hollow cage structures to be close in energies. Since ANN is built using the PBE/GGA level theory with plane wave basis set, the structures predicted by ANN are consistent with the PBE functional and plane wave basis set. From Figure

2(a), ANN predicts not only hollow cage structures but also pyramidal structures in its low-lying database.

In the case of Au_{58} , ANN potential is predicting a core surface structure, containing 10 atoms in the core and 46 atoms in the surface with C_4 symmetry as GM. The low lying isomers predicted by ANN potential are re-optimized at DFT and are shown in Figure 2(c). Gong *et al.*⁷² reported that the 10-atom core with C_1 symmetry is the lowest energy structure (II) as shown in Figure 2(c). Structure with 9-atom core is 0.67 eV high in energy and 11-atom core structure is 0.67 eV high in energy compared to 10-atom core structure (II) at the PW91/GGA level of theory.⁷² Later, Jiang *et al.*²⁹ reported a different 10-atom core structure (I) with C_4 symmetry as the GM at the TPSS level of theory. In the present study we predicted structure (I) as GM both at ANN and DFT. Structure (II) is 0.20 eV higher in energy compared to GM. ANN also predicted a 9-atom core (III) and a different 10-atom core structure (IV) in the low lying populations. Structure (III), a 9-atom core structure, is 0.34 eV higher in energy from GM which is consistent with 9-atom core structure predicted at the TPSS²⁹ level of theory. We did not observe structures with 12, 11, and 8-atom core in the low lying population. 12-atom and 8-atom core structures predicted by Gong *et al.* are around 1 eV higher in energy from the GM. Therefore, for Au_{58} , it can be concluded that ANN predicted structures are almost consistent with the previous DFT results.

In the case of Au_{34} , ANN predicted a 3-atom core structure, which is 0.2 eV lower in energy compared to 4-atom core structure. We re-examined 3-atom core structure at DFT and found that the 3-atom core structure is indeed 0.2 eV lower in energy compared to the 4-atom core. Therefore the relative energies of low lying isomers predicted by ANN are consistent with DFT predicted values. The low lying isomers are shown in Figure 2(b). The low lying isomers contain a 3-atom core structure (I), a 2-atom core structure (II), and a 4-atom core structure (III). Structures (IV, V, and VI) are 3-atom and 4-atom core structures with different surface arrangements. For neutral Au_{34} , Vargas *et al.*³⁵ used a four atom core structure (III) as the initial structure to run BOMD at the PBE/GPW level of theory. All the other previous studies, where the global optimizations were performed, were on Au_{34}^- systems and predicted 4-atom core as GM structure.⁴⁵ It was also reported that from Au_{32} to Au_{35} , in the anionic form, 3-atom core and 4-atom core structures dominate the low lying populations.⁵⁹

In the case of Au_{20} , we obtained a cage-like structure instead of a pyramidal structure. Although the cage-like structure is about 0.7 eV lower in energy than the pyramidal structure, according to DFT it is 1.12 eV higher in energy than the pyramidal structure. One of the possible reasons for this failure is that few structures of Au_{20} were included in the data set compared to Au_{17} , Au_{34} , and Au_{58} , and hence these Au_{20} structures are not well fitted and the weights are more biased towards other configurations included in the data set. We firmly believe that ANN predicts accurate or near accurate structures for Au_{17} , Au_{34} , and Au_{58} sized nanoparticles as the data set has an ample amount of these configurations. The GM for Au_{17} , Au_{34} , and Au_{58} are plotted in Figure 3. Cartesian coordinates of GM predicted using ANN for Au_{17} , Au_{20} , Au_{34} , and Au_{58} are given in the [supplementary material](#).

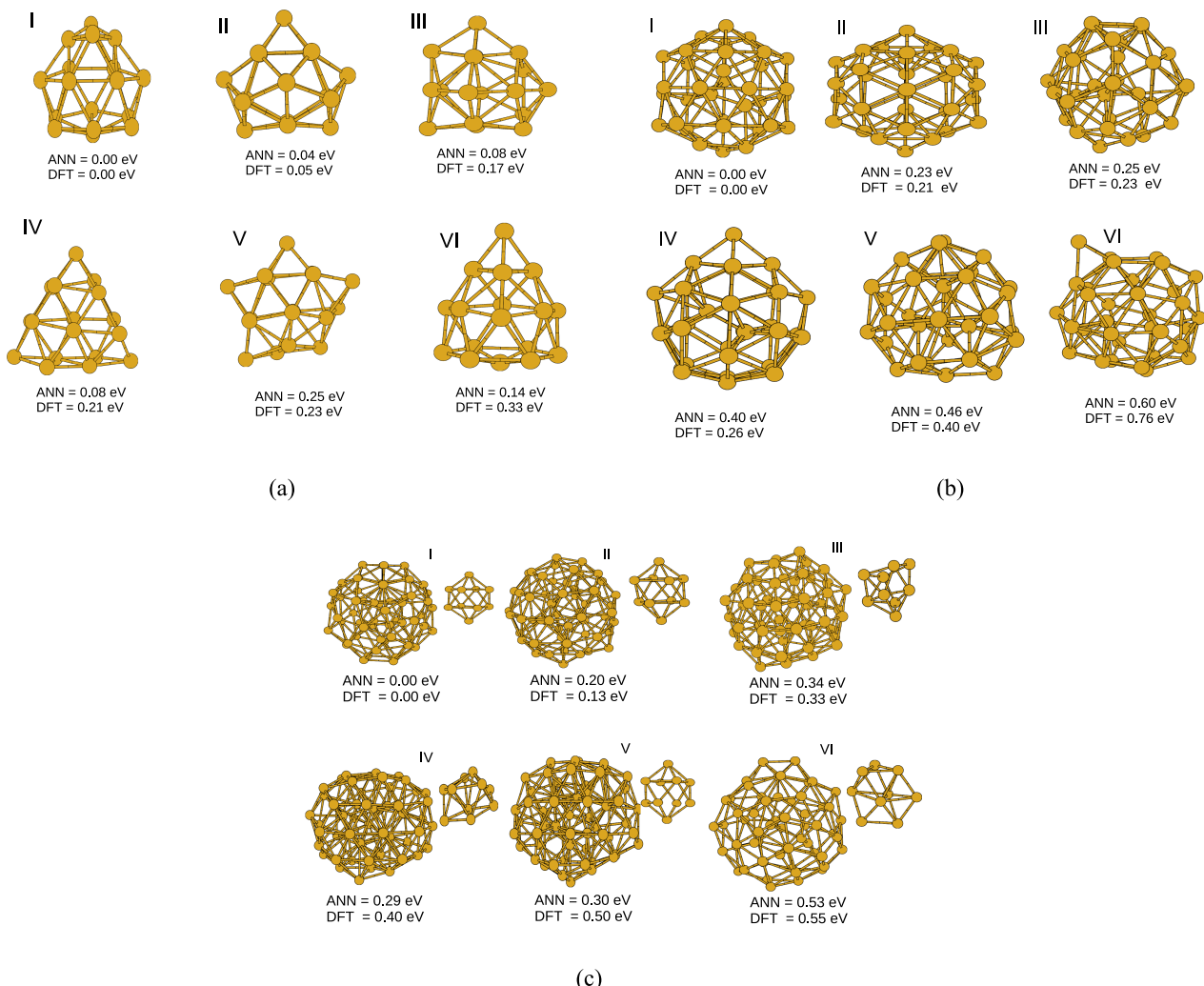


FIG. 2. Low energy isomers for (a) Au₁₇, (b) Au₃₄, (c) Au₅₈. The energy values (in eV) of each isomer relative to GM with ANN potential and DFT level.

B. Accuracy of ANN potential at high temperature

To test the accuracy of our ANN potential at high temperatures, we ran MD simulation (single trajectory) using NVT ensemble at 750 K temperature each for Au₁₇, Au₃₄, and Au₅₈. From these trajectories, we have collected 50 structures at every 40 000 steps of MD simulations in such a way that there are no correlations in structures collected. We calculated the DFT energies and ANN energies for these structures. The plot, energy versus index of structures for Au₃₄ nanoparticle, is shown in Figure 4. Similar plots for Au₁₇ and Au₅₈ are shown in

the [supplementary material](#). During training we have achieved an average root mean square error of energy, for test set, of 9.0 meV/atom. In all the plots, ANN potential is predicting energies close to DFT energies. The relative pattern between ANN and DFT throughout the simulation is reasonably in good agreement, and the error is within the 9.0 meV/atom threshold.

C. NVT MD simulations

For a complete understanding of melting process in Au nanoparticles, we performed both canonical and micro-canonical MD simulations. For all the simulations, a time step of 0.1 fs was used. From the global optimizations, the structures with lowest energy obtained were selected as the starting configurations for running MD simulations. In this study, melting analysis was done using the multiple histogram method for both NVT and NVE. [73–76](#)

In the case of NVT ensemble, the histograms were generated by performing MD simulations at 21 different temperatures ranging from 150 K to 1300 K for Au₁₇ and at 26 different temperatures ranging from 200 K to 1400 K for Au₃₄ and Au₅₈.

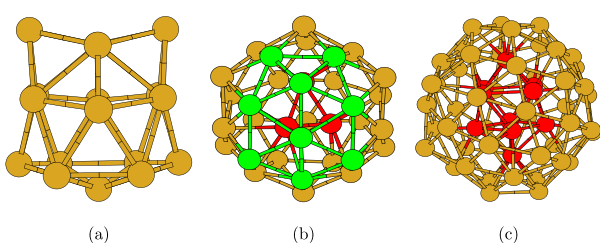


FIG. 3. GM structures (a) Au₁₇, (b) Au₃₄, (c) Au₅₈.

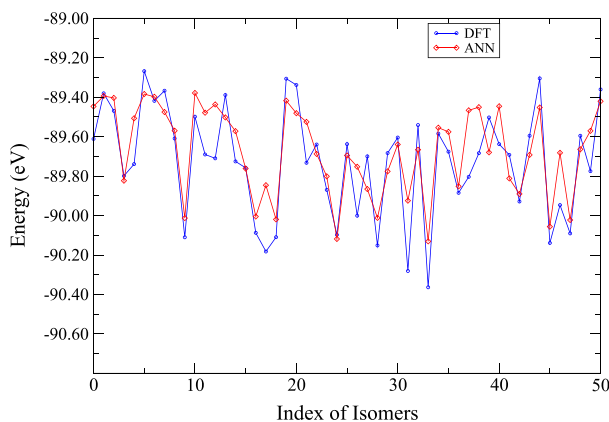


FIG. 4. Comparison of DFT and ANN potential energies during NVT simulation at 750 K temperature for Au_{34} .

Two million (2×10^6) MD steps were performed for temperatures below 700 K and one million (1×10^6) MD steps for temperatures higher than 700 K. The total simulation time of around 3 ns for Au_{17} and 3.6 ns for Au_{34} and Au_{58} . The first 30% of these moves are ignored in calculating statistical averages in order to allow thermal equilibration. The heat capacities C_v (in eV/K) as a function of temperature T (in K) for Au_n nanoparticles are plotted in Figure 5.

For Au_{17} , our results indicate peaks at 480 K and 800 K. The peak around 480 K is due to solid-solid transition, where the cage is still preserved. At 800 K, we can see the main melting peak, where the transition from cage structure to a more amorphous structures takes place. DFT based MD simulations⁷⁷ for Au_{17} shows a peak around 500 K and the main melting peak at 800 K, which is in good agreement

with that obtained using ANN potential because of identical ground state geometries. The position of shoulder peak at 480 K obtained using ANN is 20 K lower as compared to that obtained from DFT. It should be noted that the multiple histogram method is usually sensitive to a number of temperatures which are used to construct histograms. Overall, for Au_{17} , ANN potential reproduces melting curves obtained using DFT method, which is evident from peak position and broadness of peaks.

Au_{34} is a core-surface structure, where 3 core atoms form a triangle and rest are surface atoms. We observed two distinct patterns on the surface: (a) 6-membered ring with one Au atom at the center of the ring and (b) 5-membered ring with one central Au atom. In Figure 3(b) we coloured atoms on the surface with green which shows a 6-membered and a 5-membered ring pattern for better visualization. The core atoms are coloured red.

At $T = 350$ K, 3-atom core is intact and undergoes slight rotation during the course of simulation. Because of slight rotation, one of the core atoms gets coordinated with one or two surface atoms. The average coordination numbers and the average distances between atoms on the surface, between atoms of core, and between atoms of surface and core were discussed in detail in an earlier study using Born-Oppenheimer MD on Au_{34} .³⁵ The initial structure used in Born-Oppenheimer MD was a 4-atom core structure. The study concluded that in the case of Au_{34} , the core and the surface behave as separate units and also indicated that mobility of core atoms is much higher than that of surface atoms. Such behaviour of core and surface was also predicted in theoretical and experimental studies on thio-protected gold nanoparticles.^{78–80} In the present study we found a similar behaviour for the 3-atom

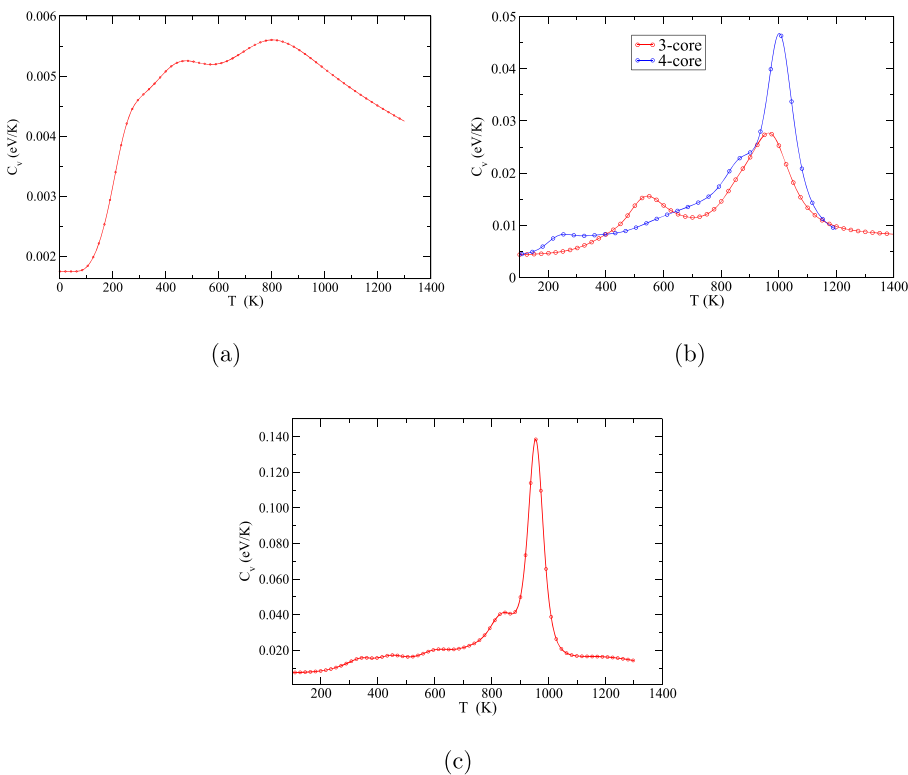


FIG. 5. Heat capacity of (a) Au_{17} , (b) Au_{34} , (c) Au_{58} .

core Au_{34} . This confirms that ANN potentials predicts dynamical properties similar to that obtained by *ab initio* studies. We plot average fluctuation in distances for surface-surface, core-core, and core-surface atoms. Figure 6(a) clearly shows that fluctuations in distances for core-surface are greater than core-core and surface-surface. Due to small fluctuations in distances for surface-surface atoms the central Au atom (which is situated at the centre of 5 or 6 membered ring) may convert to a capped atom for a 5-membered ring or may lead to a void by breaking the bond with one of 6-membered ring atoms, thereby lowering the coordination number. This feature may be presented as a surface defect, which occurs due to strong oscillations of core atoms towards surface atoms.

For $T = 550$ K, we see strong oscillatory motions between the surface and core atoms thereby increasing the effective coordination number of core atoms. At 60 ps, the core triangular unit breaks and the core atoms move on to the surface. At 33 ps, a strong peak shown in Figure 6(b) (blue curve) confirms the breaking of core-core bond. Once the bond breaks, three core atoms gradually move on to the surface. Simultaneously, the exchange of core and surface atoms takes place leading to 2-atom core structures. In Figure 6(b), above 60 ps, very strong fluctuations in core-surface (red curve) and strong fluctuations in surface-surface (green curve) confirm our observation. The heat capacity peak at 550 K, represents the solid-solid structural transition to different core structures (3-atom core to 2-atom core). At 650 K the exchange between surface and core atoms leads to formation of the 4-atom tetrahedral core structure. At first, the core-core bond is broken followed by two core atoms moving on to the surface. Simultaneously, two different surface atoms move in to the core forming a tetrahedral structure. We observe that there is a coexistence of structures with different core atoms in this temperature interval. Here, coexistence means that nanoparticles in solid-like regions may visit the liquid-like region and come back to the solid-like region. At 890 K, all the core atoms moves on to the surface to form an amorphous structure and complete melting occurs by opening of the amorphous structure at 960 K temperature.

The heat capacity curve calculated using the multiple histogram method with the 4-atom core as the initial structures in MD simulations at different temperatures is shown in Figure 5(b) (blue curve). The main melting peak at 1000 K coincides with the second melting peak of 3-atom core structure. This shows that the 4-atom core prefers to be a stable structure even at very high temperatures (upto 750 K), and gradually all 4 atoms move on to the surface and finally melts.

Interestingly, we did not find any conversion of 4-atom core to either 3-atom or 2-atom core during entire simulation. Therefore, the peak due to solid-solid transition, which is observed at 550 K for 3-atom core structure, is not present in the 4-atom core structure.

The thermodynamics of Au_{58} reveals that the melting occurs at 955 K. The simulation is started from the GM structure which consists of 10 atom BSA as the core unit surrounded by 48 surface atoms. At 350 K temperature, small rotations of the core unit are observed. There is no structural deviation at this temperature. Large fluctuations in average distance between core and surface atoms are observed which is similar to the observation in Au_{34} . At 450 K temperature, there is coexistence between BSA and distorted BSA structures. At 650 K, there is an exchange of atoms from core to surface and surface to core. The number of core atoms is changed from 10 to 9 atoms. The core and outer surface are clearly recognisable as different layers of structure at this temperature. The melting starts at temperature of around 850 K, where complete mixing of core and outer surface atoms can be seen and all the atoms start to diffuse.

Order parameters like volume of a nanoparticle, predicted using Equation (14), gives valuable information for studying phase transitions in nanoparticles,

$$V = \frac{4}{3}\pi \left[\left(\frac{5}{2M} \right)^{3/2} \sqrt{I_A I_B I_C} \right], \quad (14)$$

where M is total mass and I_A, I_B, I_C are three principle moments of inertia of nanoparticle. In Figure 7 volume of nanoparticles is plotted against temperature for Au_{17} (in black), Au_{34} (in green), and Au_{58} (in red). For Au_{17} , there is a slow increase in volume of the nanoparticles with increase in temperature. There is no exact temperature where we can notice considerable change in volume. This is similar to the broadness in heat capacity curve observed in Figure 5(a). Such transitions indicate a second order phase transition. For Au_{58} , above 900 K, a sudden jump in volume leading to liquid-like state can be observed. Therefore, the physical properties such as narrow heat capacity curve and sudden increase in volume of nanoparticle indicate a first order phase transition. Properties for Au_{34} lie in between Au_{17} and Au_{58} . A gradual increase in volume over a broad temperature range is observed. Due to finite size effects, the phase transition of nanoparticles involves broad melting range leading to coexistence phenomena.^{49–52} One way to recognize the coexistence

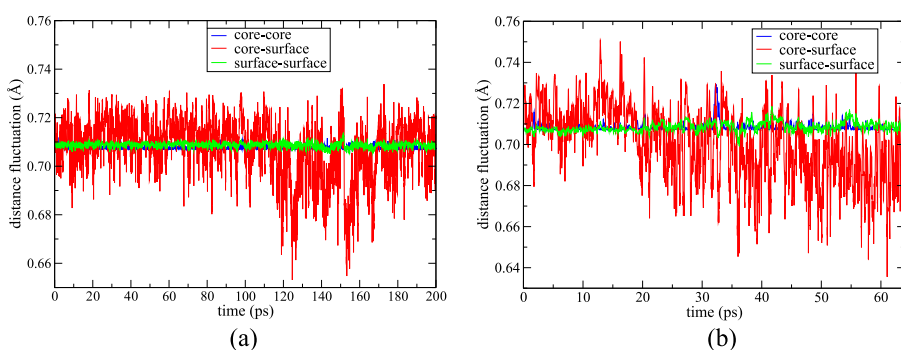


FIG. 6. Distance fluctuations of Au_{34} at (a) 350 K and (b) 550 K.

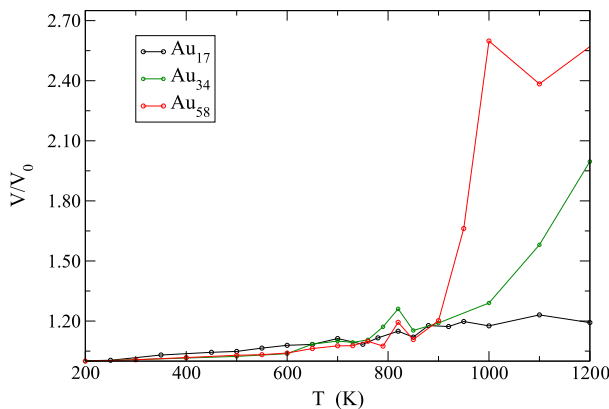


FIG. 7. Average volume of nanoparticle at different temperature simulations.

phenomena in small nanoparticles is by evaluation of equilibrium constant between solid-like and liquid-like phases.

Recently, a simple method was proposed for the calculation of equilibrium constant (K_{eq}) for the study of phase transition in Ni₅₅ nanoparticle.⁵⁸ For the bulk system, the solid-liquid equilibrium can be characterized within the system at same time in a time trajectory. This is not possible for a nano-system because we cannot distinguish solid and liquid within a nanoparticle at the same time, which means that solid-liquid equilibrium should be understood in terms of time spent by a nano-system in the solid state and in the liquid state. Therefore, K_{eq} is defined as the ratio of time fraction of nanoparticle in the liquid state (t_l) to the time fraction of nanoparticle in the solid state (t_s): $K_{eq} = \frac{t_l}{t_s}$. To evaluate the time fractions, we begin with the thermodynamic equilibrium where $\Delta G = 0$. If we assume constant external pressure, then $\Delta E = T\Delta S$, where $E (=H$ at constant pressure) is an internal energy of solid or liquid state. At phase transition, we can write $\Delta S = \frac{\Delta E_f}{T}$ for a bulk system, and for a nano-system it can be written as $\frac{t_l \Delta E_f}{T}$. The time fraction in the liquid state is therefore given by

$$t_l = \frac{\Delta E}{\Delta E_f}. \quad (15)$$

Enthalpy of fusion, ΔE_f , is taken as difference between solid extrapolated line and liquid extrapolated line at the phase transition in Figure 8(a) for Au₃₄ and Figure 8(b) for Au₅₈. The time fraction in the solid state is given by $1 - t_l$. For Au₃₄, as shown in Figure 8(c), below 600 K, the value of t_l is below 0.3. Below 600 K, nanoparticle spends most of its time in the solid region. Between 800 K and 1100 K we see a gradual increase in time fraction in liquid from 0.4 to 0.9. Actual melting occurs in this region as shown in the caloric curve in Figure 8(a) and also in the heat capacity curve in Figure 5(b). From Figure 8(e), the value of K_{eq} between 800 K and 960 K shows a gradual increase, which shows that nanoparticle gradually prefers to be in the liquid state longer than the solid state. Above 1000 K, we can see a steep increase in K_{eq} , which shows that the liquid state is the only preferred state. In the case of Au₅₈, the caloric curve in Figure 8(b) between 850 K and 1000 K can be considered as the melting region. The peak of heat capacity curve 5(c) is around 955 K. A steep increase in time fraction in liquid from 0.5 to 0.9 between 900 K and 1000 K confirms that the nanoparticle spends longer time in liquid state

compared to the solid state. From Figure 8(f), K_{eq} values around 950 K starts to increase gradually, showing the preference for liquid state. We selected MD trajectories at two different temperatures for Au₃₄ and Au₅₈ and calculated volume variations along the MD trajectory. For Au₃₄, at 350 K (red curve), as shown in Figure 9, there is no large variation in volume and the nanoparticle remains in the solid-like phase. At 860 K (blue curve), the nanoparticle is in the solidlike region initially for the first 20 ps. It then spends time in the liquidlike region for 20 ps before coming back to solidlike region again. We have shown the solidlike structures labelled as (a), (c), (e), and (g) (with core atoms) and liquidlike structures labelled as (b), (d), and (f) in Figure 9. Similarly, in the case of Au₅₈, the plot of volume with respect to time at 550 K (red curve) and 920 K (blue curve) is shown in Figure 10. At 550 K, nanoparticle is always in solidlike region, which is evident from Figure 10. At 920 K temperature, it can be shown that nanoparticle spends time in solidlike region for 16 ps, and then it spends time in liquidlike region for 25 ps. The solidlike structures labelled as (a) and (c) and liquidlike structure labelled as (b) are shown in Figure 10.

From the above studies, in NVT ensemble for Au₃₄ and Au₅₈, following conclusions can be drawn. (1) Au nanoparticles show a broadened melting transition, which is similar to other metal nanoparticles, due to finite size effects. (2) No premelting is observed in Au nanoparticles due to absence of surface melting. We noticed that in Au nanoparticles the core atoms diffuse to the surface with an increase in temperature. The surface layer is rigid as compared to that of core. Defects in surface layer occur due strong oscillatory motions of core atoms. This study clearly shows that melting in gold cluster starts from core to surface, unlike other metal clusters, like Al and Na, where melting starts from surface atoms. (3) Dynamic coexistence exists in the melting range. (4) Dynamic coexistence in the melting range is characterized by evaluating equilibrium constant which shows that in the melting range, the solidlike and liquidlike phases are in equilibrium and with increase in temperature, nanoparticles prefer to spend longer time in the liquid region. (5) Variation in volume of the nanoparticle clearly shows the coexistence of solidlike and liquidlike phases in the melting region.

D. NVE MD simulations

NVE ensemble is an appropriate theory if we consider a totally isolated system and if we want to carefully consider all the subtle changes that occur during the melting process in the isolated system.^{51,81,82} Here we intend to use the NVE ensemble to study the melting process in Au nanoparticles. It should be noted that physical properties such as heat capacity may not be equivalent for different statistical ensembles, NVT and NVE, due to finite size effects. Therefore, we cannot directly compare the characteristic features of melting such as peak position, width of the peak, and in particular the caloric curves obtained from NVT and NVE. Negative heat capacities have been predicted in NVE ensemble in the melting range of nanoparticles. This is evident from the caloric curves, where energy vs temperature plot shows a S-bend, such that there is a decrease in temperature with increase in energy. It has been

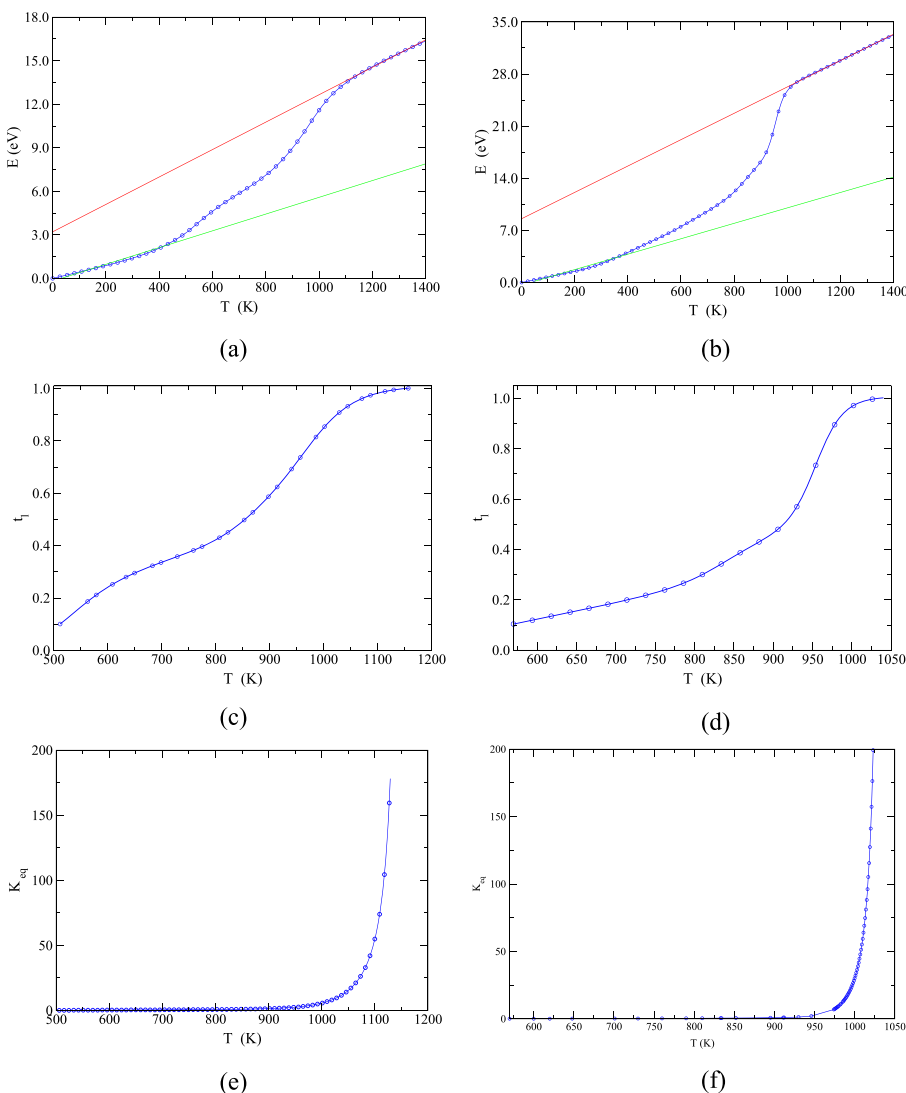


FIG. 8. (a) Caloric curve for Au_{34} , (b) caloric curve for Au_{58} , (c) time fraction in liquid for Au_{34} , (d) time fraction in liquid for Au_{58} , (e) equilibrium constant for Au_{34} , (f) equilibrium constant for Au_{58} .

proved, using simple models,⁸³ that S-bend is a natural consequence of isolated systems in NVE ensemble. S-bends have been predicted for small Na nanoparticles both experimentally⁵¹ and theoretically.⁸⁴ Therefore, we study the presence of S-bend in the caloric curve for Au_{17} , Au_{34} , and Au_{58} . This requires constructing a caloric curve using the NVE ensemble for Au nanoparticles. For this, we again used multiple histogram method for evaluating the configurational entropy. It has been shown earlier that the caloric curve obtained using configurational entropy and potential energy is similar to that obtained using total entropy and total energy.⁷⁶ Hence, the histograms were generated by performing MD simulations at 21 different potential energies ranging from 1.08 eV to 5.0 eV for Au_{17} and at 29 different potential energies ranging from 1.34 eV to 15.0 eV for Au_{34} and 3.5 eV to 21.0 eV for Au_{58} . Figure 11 shows caloric curves obtained for all the three nanoparticles discussed using $T = 1/\frac{\partial S}{\partial E}$. Two million (2×10^6) MD steps are performed for each energy which corresponds to a total simulation time of around 3 ns for Au_{17} and 3.9 ns for Au_{34} and Au_{58} . The first 30% of these moves are ignored in calculating statistical averages to allow thermal equilibration. Figure 11 shows the presence of S-bend for Au_{17} , Au_{34} , and

Au_{58} . The caloric curves are constructed using temperature that is defined in terms of microcanonical entropy, $T = 1/\frac{\partial S}{\partial E}$. The caloric curve derived using temperatures based on average kinetic energy is shown in the [supplementary material](#). It should be noted that both these definitions of temperature are not equivalent in NVE simulations.

Using microcanonical temperature, $T = 1/\frac{\partial S}{\partial E}$, we tried to recognize the phase coexistence at a fixed energy on the caloric curve where the nanoparticle fluctuates between solidlike and liquidlike phases. We plot the volume of the nanoparticle along the trajectory to recognize the structural fluctuations occurring during coexistence. In the case of Au_{17} , we observe a small S-bend around 1000 K. Using kinetic definition of temperature, no S-bend is observed for Au_{17} (see figure in [supplementary material](#)). It should be noted that for small system it becomes increasingly difficult to distinguish the structures between solidlike and liquidlike phases.

In the case of Au_{34} , the trajectory obtained at $E_3 = 7.08$ eV, which is at the centre of S-bend, was identified to visualize phase coexistence. We found that the nanoparticle indeed spends about 50 ps in solidlike regions (nanoparticle with core atoms) before going to liquidlike region (nanoparticles

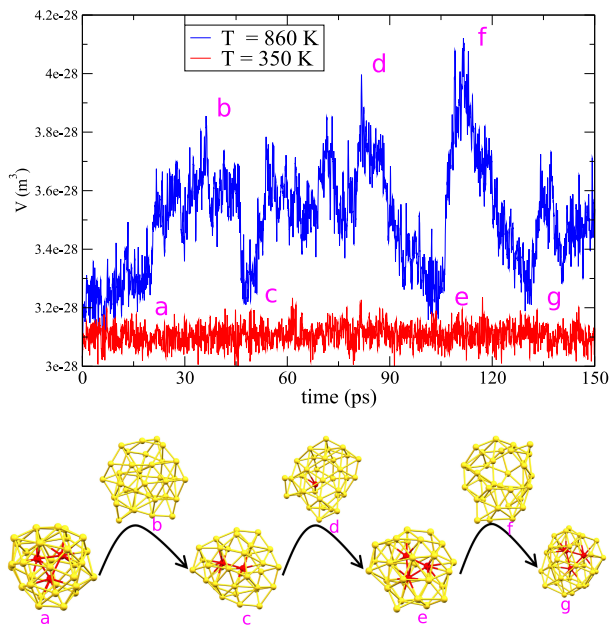


FIG. 9. Volume variation of Au_{34} along MD trajectory and the corresponding structures in coexistence region.

opens up) followed by visiting the solid region again. From the volume plot shown in Figure 12, the black curve represents the solid phase which was obtained at energy $E_1 = 3.32$ eV. The green curve represents the coexistence region which was obtained from the trajectory that was considered at the centre of S-bend. It is clear from the plot that in the coexistence region the nanoparticles fluctuates between solidlike and liquidlike states. We visualised the trajectory and found that the

3 atom core was converted to 2 and 4 atom core structures by exchanging of atoms from core to surface and surface to core. Gradually all the core atoms were moved to the surface completely by forming liquidlike structures that have no structural feature. After visiting liquid like structures, again it is coming back to solidlike structure (containing core atoms) with distorted outer surface.

For Au_{58} , a similar observation is made when the trajectory at the centre of S-bend is used to explain phase coexistence. We observed the formation of different core surface structures with different number of core atoms (9, 8, and 7 atoms). There is exchange of atoms from core to surface and surface to core. Solidlike structure converts to liquidlike structure, having no core atoms and no structural features, and the nanoparticles remain in such a liquidlike state for almost 74 ps. The nanoparticles then reappear in the solidlike state for 67 ps. This is clearly evident from the volume plot as shown in Figure 13.

Following conclusions can be made from the NVE simulations. If microcanonical definition for temperature was considered, then we observed S-bend in all the three nanoparticles, which leads to negative heat capacity. Therefore, one may assume that negative heat capacity is a natural consequence for NVE simulations for medium sized Au nanoparticles. In NVE the fluctuations between solidlike and liquidlike structures can be explicitly visualized as core and open structures, respectively. Caloric curves of NVT and NVE differ for all the systems considered in this study. It is interesting to note that nanoparticle spends longer times in liquidlike and solidlike regions for NVE ensemble when compared to that of NVT ensemble.

E. Probability of isomers at finite temperature

For probing the structure of a nanoparticle by exploring potential energy surface, the commonly used computational techniques include a search algorithms in combination with a local optimization tool. Such techniques are used to predict low lying isomers and the GM isomer at $T = 0$ K. At very low temperatures, usually near $T = 0$ K, the GM structure can be considered as the most probable structure because the lowest potential energy will lead to a larger Boltzmann term that has contributions. But in the case of finite temperature it is just not the potential energy and the temperature that determines probability of particular isomer. One has to consider electronic, vibrational, and rotational contributions to the partition functions at finite temperatures. Here we calculate probability of each isomer at finite temperatures according to the following:

$$P_{iso} = \frac{\exp\left(\frac{-\Delta E_{RP}^{iso}}{K_B T}\right) q_{rov}^{iso} q_{ele}^{iso}}{\sum_{iso} \exp\left(\frac{-\Delta E_{RP}^{iso}}{K_B T}\right) q_{rov}^{iso} q_{ele}^{iso}}, \quad (16)$$

where ΔE_{RP}^{iso} is the relative potential energy of isomer from GM. q_{rov}^{iso} and q_{ele}^{iso} are rotational vibrational partition function and electronic partition function of particular isomer. In the above formula, electronic partition function can be safely omitted because the excited state energy levels usually have negligible contribution to the partition function.^{55,85–87} For calculating the rotational contributions we adopted classical

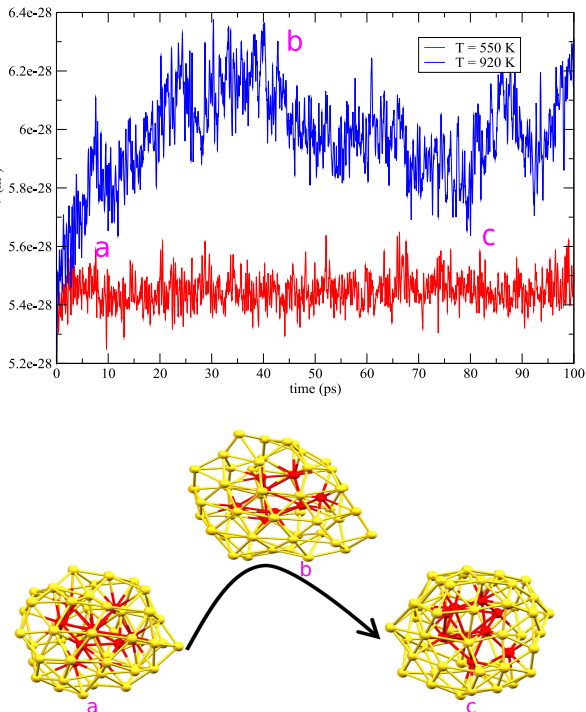


FIG. 10. Volume variation of Au_{58} along the MD trajectory and the corresponding structures in coexistence region.

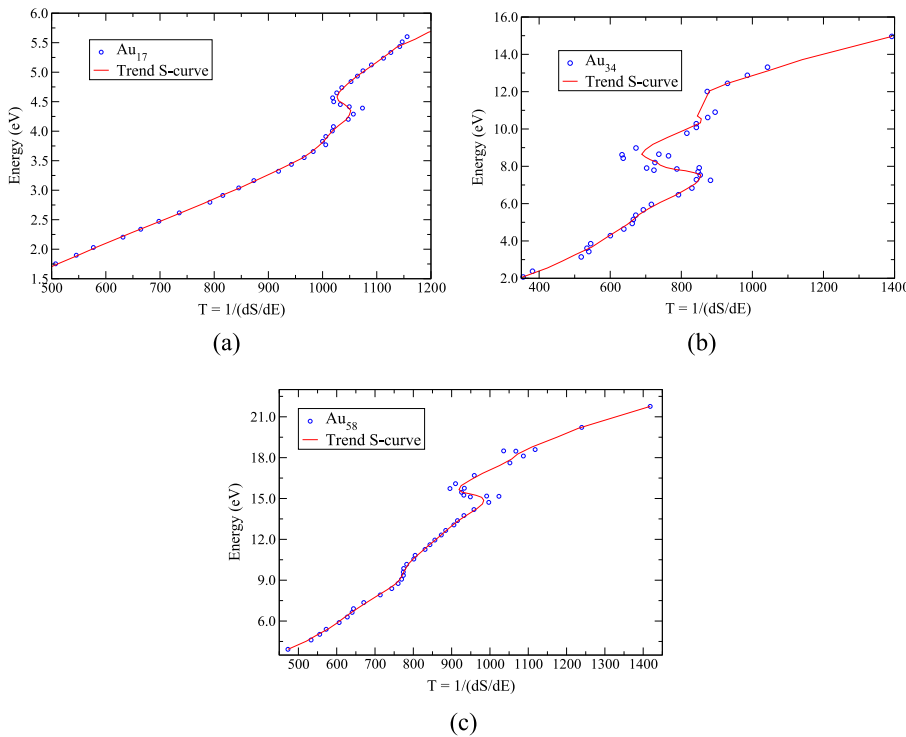


FIG. 11. Caloric curves of NVE ensemble (a) Au_{17} , (b) Au_{34} , (c) Au_{58} .

rigid rotor approximations. And for calculating the vibrational contributions we adopted harmonic approximations,

$$p_{iso} = \frac{\exp\left(\frac{-\Delta E_{RP}^{iso}}{K_B T}\right) q_{rov}^{iso}}{\sum_{iso} \exp\left(\frac{-\Delta E_{RP}^{iso}}{K_B T}\right) q_{rov}^{iso}}, \quad (17)$$

$$q_{rov}^{iso} = q_{rot}^{iso} q_{vib}^{iso}, \quad (18)$$

$$q_{rot}^{iso} = \left(\frac{8\pi^2}{\beta h^2}\right)^{3/2} \frac{\sqrt{I_A^{iso} I_B^{iso} I_C^{iso}}}{\sigma^{iso}}, \quad (19)$$

$$q_{vib}^{iso} = \prod_m \frac{\exp\left(\frac{-hc\tilde{\nu}_m^{iso}}{2K_B T}\right)}{1 - \exp\left(\frac{-hc\tilde{\nu}_m^{iso}}{K_B T}\right)}, \quad (20)$$

where I_A^{iso} , I_B^{iso} , and I_C^{iso} are the three principle moments of inertia and $\tilde{\nu}$ is the wave number of m th normal mode for an isomer. For each nanoparticles we selected two different temperatures to calculate probability. One is at room temperature and the other is near melting temperature (T_m).

We started by considering all the isomers that are below 0.5 eV from GM at $T = 0$ K for Au_{34} and Au_{58} . In the case of Au_{34} , we collected 120 isomers and used 50 isomers to calculate the probability at different temperatures. The probability

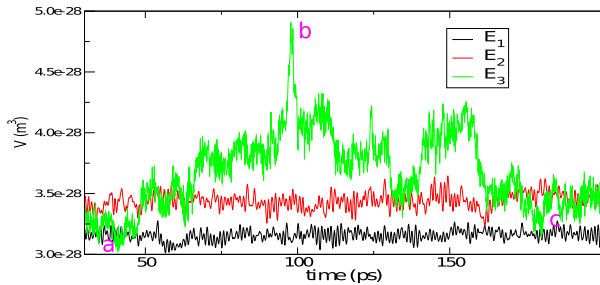


FIG. 12. Volume variations of Au_{34} at $E_1 = 3.32$ eV, $E_2 = 5.34$ eV, and $E_3 = 7.08$ eV using NVE MD and their corresponding structures in the S-bend region.

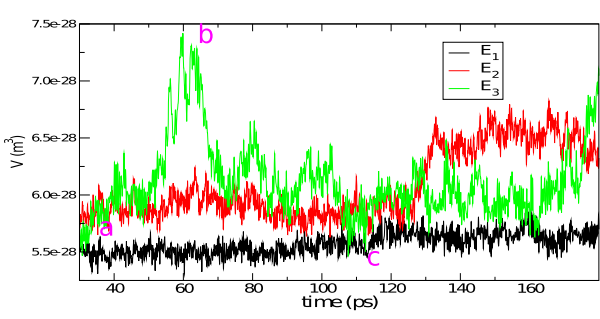


FIG. 13. Volume variations of Au_{58} at $E_1 = 9.90$ eV, $E_2 = 12.65$ eV, and $E_3 = 14.01$ eV in NVE MD and their corresponding structures in the S-bend region.

TABLE III. Probability of 5 lowest isomers of Au₃₄.

| T (K) | P ₁ (%) | P ₂ (%) | P ₃ (%) | P ₄ (%) | P ₅ (%) |
|-------|--------------------|--------------------|--------------------|--------------------|--------------------|
| 50 | 97.0 | 2.0 | 0.0 | 0.0 | 0.0 |
| 150 | 62.0 | 18.0 | 1.0 | 2.0 | 1.0 |
| 250 | 26.0 | 12.0 | 1.6 | 4.8 | 5.2 |
| 350 | 13.0 | 7.0 | 1.5 | 4.3 | 6.0 |
| 550 | 5.0 | 3.0 | 1.10 | 3.2 | 5.7 |

plot for all 50 isomers at different temperatures is shown in the [supplementary material](#). In Table III, we show top 5 isomers that are more probable, including GM, to understand the variations in probability at different temperatures. P₁, the GM with 3-atom core, contributes to 97% at T = 50 K, which means that at very low temperature GM dominates because the potential energy of isomer is a dominating factor in partition function at very low temperatures. As the temperatures is increased the probability of GM is decreased considerably. We can see that at 250 K the cumulative probability of all the 5 isomers considered is less than 50%. This also shows the increase in number of isomers that contribute fairly to probability at 250 K and the GM alone cannot be considered for explaining the properties of nanoparticles at this temperature. At 550 K, P₁ and P₅ show similar probabilities. Here, P₅ is a structure with 4 atom core as shown in Figure 14(e). Interestingly in the heat capacity curve there is structural transition from 3-atom core to 4-atom

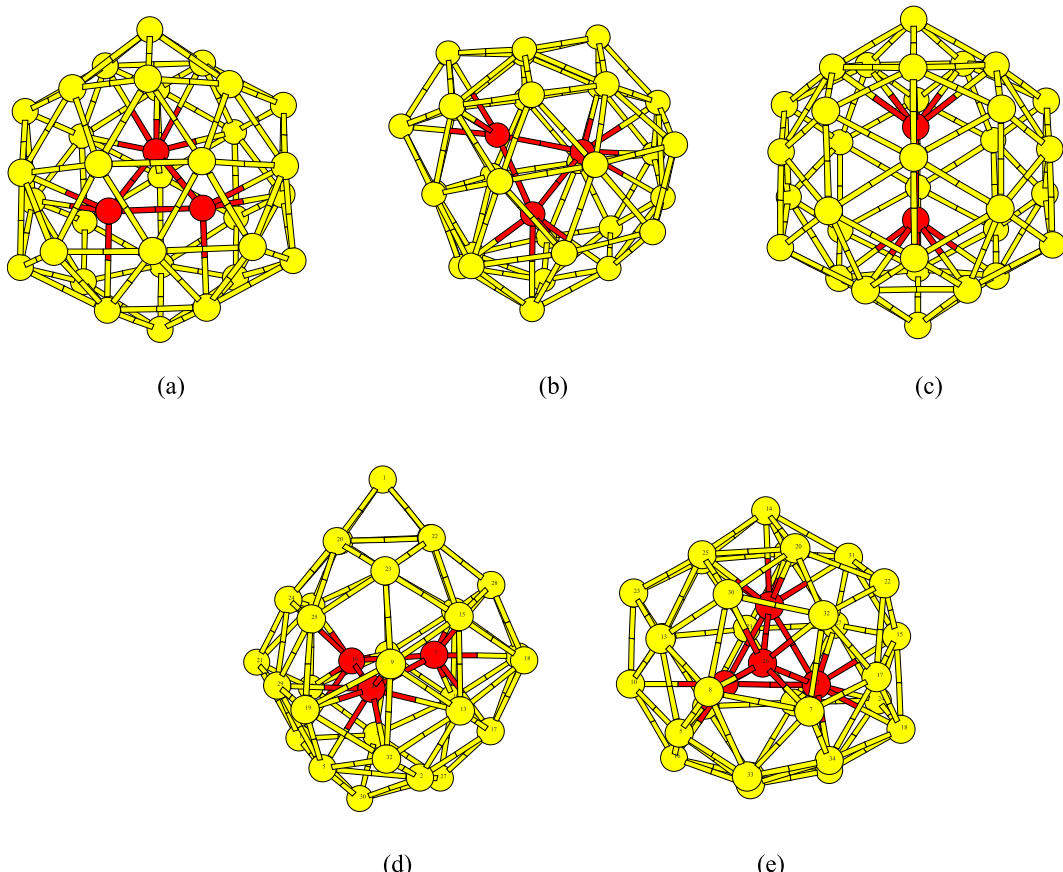
core at 550 K via 2-atom core. In the case of Au₅₈, we can see that GM structure is dominant till 350 K, which means that the core structure is still intact. Therefore for Au₅₈, unlike Au₃₄, GM structure can be used to represent properties of the nanoparticles at this temperature. Only near melting range we see that the probability of GM drops considerably as shown in Table IV and the properties can no longer be represented by GM. The corresponding structures for Au₅₈ are shown in Figure 15.

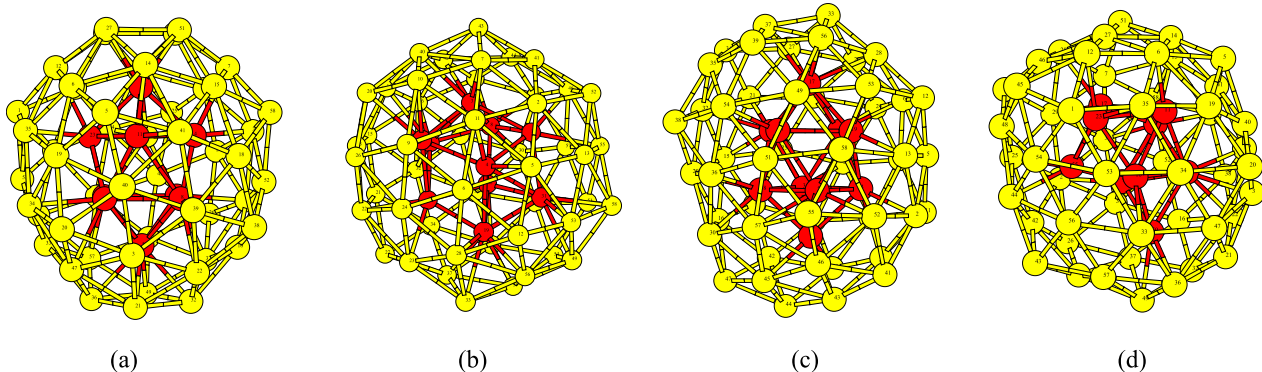
The contributions from all the isomers considered in this study, which are 0.5 eV higher in energy from GM can be visualized by calculating isomeric energies. Isomeric energies (E_{Isomeric}) are obtained using the following:

$$E_{\text{Isomeric}} = - (E_{\text{vib}}^{\text{GM}} + E_{\text{rot}}^{\text{GM}}) + \sum_{\alpha=\text{isomers}} (\Delta E_{\text{RP}}^{\alpha} + E_{\text{vib}}^{\alpha} + E_{\text{rot}}^{\alpha}) P_{\alpha}, \quad (21)$$

TABLE IV. Probability of 4 lowest isomers of Au₅₈.

| T (K) | P ₁ (%) | P ₂ (%) | P ₃ (%) | P ₄ (%) |
|-------|--------------------|--------------------|--------------------|--------------------|
| 50 | 99.0 | 0.0 | 0.0 | 0.0 |
| 150 | 71.0 | 6.1 | 0.0 | 0.0 |
| 250 | 51.0 | 9.5 | 0.0 | 0.0 |
| 350 | 18.0 | 7.5 | 2.3 | 1.0 |
| 800 | 7.1 | 3.5 | 3.9 | 2.7 |

FIG. 14. Most probable structures of Au₃₄ (a) P₁, (b) P₂, (c) P₃, (d) P₄, and (e) P₅.

FIG. 15. Most probable structures of Au_{58} (a) P_1 , (b) P_2 , (c) P_3 , and (d) P_4 .

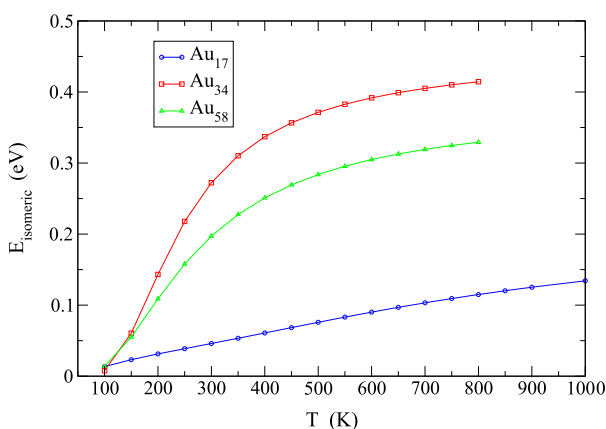
where E_{vib}^{GM} and E_{rot}^{GM} are vibrational and rotational energies of GM. ΔE_{RP}^a is the relative potential energy of isomer from GM and P_a is the probability of isomer at particular temperature. In Figure 16, isomeric energies of Au_{17} , Au_{34} , and Au_{58} are plotted against the temperature. In the case of Au_{34} , it is evident that GM or any one structure cannot be used to represent properties of nanoparticle at temperatures greater than 250 K. This is true since at 250 K the cumulative probability of 5 dominant isomers is less than 50%. The sharp increase of isomeric energy to 0.37 eV shows that high energy isomers make significant contributions to average properties of nanoparticle. In the case of Au_{58} at 300 K, the isomeric energy is about 0.19 eV which shows that GM structure is still a good candidate for calculating ensemble average properties of nanoparticle. Therefore in the case of Au_{58} the effect of GM structure ceases only at very high temperatures (≥ 700 K) while for Au_{34} it ceases at 250 K only. For Au_{17} there are many cage isomers with energies very close (0.003 eV) to GM and therefore the isomeric energy plot shows a flat distribution over a wide range of temperatures.

From the probability estimations and isomeric energies, we can conclude that in all the three nanoparticles considered in this study, there are many low energy isomers and the transitions between them can be achieved by increasing temperature. In the case of Au_{34} and Au_{58} , the core has greater mobility compared to that of surface atoms. Core disrupts the surface atoms

leading to dynamic change in coordination numbers of surface atoms leading to strong fluxional nanoparticle. In the case of Au_{34} , the existence of numerous structural isomers (120 isomers below 0.5 eV from GM) is due to soft surface. Atoms on surface undergo dynamic change in coordination because of strong fluctuations between the 3 atom-core and the surface around 300 K. For Au_{58} , due to the presence of a very stable core structure (BSA) the number of isomers (70 isomers below 0.5 eV from GM) is lower than that of Au_{34} . Most of the isomers obtained are due to fluxionality in the outer surface with the core structure intact at 300 K. In the case of Au_{17} , since only surface atoms are present, we can see a wide variety of cage structures leading to highly fluxional structure at room temperature. Therefore in Au nanoparticle, due to the presence of strong dynamic fluxionality, GM structure cannot be considered alone for understanding the catalytic functionality at finite temperature.

IV. CONCLUSIONS

In conclusion, we used ANN potential to study dynamics of Au nanoparticles. ANN potential is an interatomic classical potential that was obtained by fitting to DFT data of Au nanoparticles. The potential has been tested to reproduce DFT energies and forces for a test data set. We obtained an average RMSE error of 9 meV/atom for energies and RMSE error of about 88 meV/ \AA for forces. ANN reproduced the GM structure for Au_{17} and Au_{58} and predicted a new 3-core atom GM structure for Au_{34} . In terms of computational speed, the time required to evaluate energy and $3N$ forces of a nanoparticle is proportional to $N^{0.4}$ for ANN. Therefore, ANN can be suitable for studying dynamics of medium to large sized nanoparticles (500–1000 atoms) in future. It would be beneficial in terms of computational speed to parallelize NN code for treating such large particles. Using ANN, we studied the thermodynamical properties of Au_{17} , Au_{34} , and Au_{58} . NVT MD simulations were used to understand the structure property relations and melting transitions. Using fluctuations in distance indicator, we showed that the outer atomic layer for Au_{34} and Au_{58} is rigid when compared to core atoms. At around 300 K, the core atoms are responsible to change the coordination number of surface atoms, thereby creating defects on surface. Indicators such as heat capacity of nanoparticle, variation in volume

FIG. 16. Isomeric energies in finite temperature range for Au_{17} , Au_{34} , and Au_{58} .

of nanoparticle along the trajectory, and equilibrium constant were used to study the dynamic coexistence during the melting process. From the NVE MD simulations, we observed a characteristic S-bend in the calorific curve using entropic definition for temperature for all the nanoparticles considered. Both, at NVE and NVT, we predicted melting process to begin from core atoms and then go to surface atoms in Au nanoparticles studied here. Finally, we evaluated the probability of isomer and isomeric energy at finite temperatures to understand the contributions from GM and other low lying isomers to the properties of nanoparticle. In the case of Au₃₄, the GM structure has low probability at room temperature. But for Au₁₇ and Au₅₈, the GM structure still dominates at room temperature.

SUPPLEMENTARY MATERIAL

See [supplementary material](#) for the derivative of angular function, analytical force in expanded form, RMSE equations, η, ζ, λ parameters for radial and angular functions, volume plot of Au₅₈ in NVT dynamics, calorific curves derived from kinetic energy definition for temperature, probability plots for Au₁₇, Au₃₄, and Au₅₈, comparison of DFT and ANN potential energy plots during NVT simulation at high temperature for Au₁₇, Au₃₄, and Au₅₈, and coordinates for the GM structures of Au₁₇, Au₂₀, Au₃₄, and Au₅₈.

ACKNOWLEDGMENTS

We thank IIT Indore for providing server facilities and UGC for senior research fellowship. This work is supported by council of scientific and industrial research (CSIR), India.

- ¹M. Haruta, *Catal. Today* **36**, 153 (1997).
- ²M. S. Chen and D. W. Goodman, *Science* **306**, 252 (2004).
- ³M. C. Daniel and D. Astruc, *Chem. Rev.* **104**, 293 (2004).
- ⁴G. J. Hutchings, M. Brust, and H. Schmidbaur, *Chem. Soc. Rev.* **37**, 1759 (2008).
- ⁵P. Schwerdtfeger, *Angew. Chem., Int. Ed.* **42**, 1892–1895 (2003).
- ⁶P. Pyykko, *Chem. Rev.* **88**, 563 (1988).
- ⁷P. Schwerdtfeger, M. Dolg, W. H. Eugen Schwarz, G. A. Bowmaker and P. D. W. Boyd, *J. Chem. Phys.* **91**, 3 (1989).
- ⁸H. Hakkinen, B. Yoon, U. Landman, X. Li, H. J. Zhai, and L. S. Wang, *J. Phys. Chem. A* **107**, 6168 (2003).
- ⁹S. Bulusu, X. Li, L. S. Wang, and X. C. Zeng, *Proc. Natl. Acad. Sci. U. S. A.* **103**, 8326 (2006).
- ¹⁰M. P. Johansson, D. Sundholm, and J. Vaara, *Angew. Chem., Int. Ed.* **43**, 2678 (2004).
- ¹¹J. Li, X. Li, H. J. Zhai, and L. S. Wang, *Science* **299**, 864 (2003).
- ¹²J. M. Soler, E. Artacho, J. D. Gale, A. Garca, J. Junquera, P. Ordejon, and D. Sanchez-Portal, *J. Phys.: Condens. Matter* **14**, 2745 (2002).
- ¹³S. Kümmel and L. Kronik, *Rev. Mod. Phys.* **80**, 3 (2008).
- ¹⁴T. B. Blank, S. D. Brown, A. W. Calhoun, and D. J. Doren, *J. Chem. Phys.* **103**, 4129 (1995).
- ¹⁵F. V. Prudente and J. J. S. Neto, *Chem. Phys. Lett.* **287**, 585 (1998).
- ¹⁶A. P. Bartok, M. C. Payne, R. Kondor, and G. Csanyi, *Phys. Rev. Lett.* **104**, 136403 (2010).
- ¹⁷R. Fournier and S. Orel, *J. Chem. Phys.* **139**, 234110 (2013).
- ¹⁸S. Bulusu and R. Fournier, *J. Chem. Phys.* **136**, 64112 (2012).
- ¹⁹J. Behler and M. Parrinello, *Phys. Rev. Lett.* **98**, 146401 (2007).
- ²⁰J. Behler, *J. Chem. Phys.* **134**, 074106 (2011).
- ²¹J. Behler, *J. Phys.: Condens. Matter* **26**, 183001 (2014).
- ²²J. Behler, R. Martonak, D. Donadio, and M. Parrinello, *Phys. Rev. Lett.* **100**, 185501 (2008).
- ²³N. Artrith and J. Behler, *Phys. Rev. B* **85**, 045439 (2012).
- ²⁴N. Artrith, T. Morawietz, and J. Behler, *Phys. Rev. B* **83**, 153101 (2011).
- ²⁵N. Artrith, B. Hiller, and J. Behler, *Phys. Status Solidi (b)* **250**, 1191–1203 (2013).
- ²⁶N. Artrith and A. M. Kolpak, *Nano Lett.* **14**, 2670 (2014).
- ²⁷N. Artrith and A. M. Kolpak, *Comput. Mater. Sci.* **110**, 20–28 (2015).
- ²⁸T. Morawietz and J. Behler, *J. Phys. Chem. A* **117**, 7356 (2013).
- ²⁹O. Runhai, Y. Xie, and J. De-en, *Nanoscale* **7**, 14817 (2015).
- ³⁰S. chiriki, S. S. Bulusu, *Chem. Phys. Lett.* **652**, 130 (2016).
- ³¹N. Artrith and A. Urban, *Comput. Mater. Sci.* **114**, 135150 (2016).
- ³²J. S. Elias, N. Artrith, M. Bugnet, L. Giordano, G. A. Botton, A. M. Kolpak, and Y. Shao-Horn, *ACS Catal.* **6**, 1675–1679 (2016).
- ³³H. Zhai and A. N. Alexandrova, *J. Chem. Theory Comput.* **12**, 6213 (2016).
- ³⁴J. Behler, *Int. J. Quantum Chem.* **115**, 1032 (2015).
- ³⁵A. Vargas, G. Santarossa, M. Iannuzzi, and A. Baiker, *Phys. Rev. B* **80**, 195421 (2009).
- ³⁶Z. Duan, Y. Li, J. Timoshenko, S. T. Chill, M. A. Rachel, F. Yancey David, I. Frenkel Anatoly, M. Crooks Richard, and G. Henkelman, *Catal. Sci. Technol.* **6**, 6879 (2016).
- ³⁷P. Grune, D. M. Rayner, B. Redlich, A. F. G. van der Meer, J. T. Lyon, G. Meijer, and A. Fielicke, *Science* **321**, 674 (2008).
- ³⁸B. Schaefer, R. Pal, N. S. Khetrapal, M. Amsler, A. Sadeghi, V. Blum, X. C. Zeng, S. Goedecker, and L. S. Wang, *ACS Nano* **8**, 7413 (2014).
- ³⁹M. Ji, X. Gu, X. Li, X. G. Gong, J. Li, and L. S. Wang, *Angew. Chem., Int. Ed.* **44**, 7119 (2005).
- ⁴⁰D. E. Jiang and M. Walter, *Phys. Rev. B* **84**, 193042 (2011).
- ⁴¹J. Wang, J. Jellinek, J. Zhao, Z. Chen, R. B. King, and P. V. R. Schleyer, *J. Phys. Chem. A* **109**, 9265 (2005).
- ⁴²S. Bulusu, X. Li, L. S. Wang, and X. C. Zeng, *J. Phys. Chem. C* **111**, 4190 (2007).
- ⁴³X. Gu, S. Bulusu, X. Li, X. C. Zeng, J. Li, X. G. Gong, and L. S. Wang, *J. Phys. Chem. C* **111**, 8228 (2007).
- ⁴⁴A. Lechtken, D. Schooss, J. R. Stairs, M. N. Blom, F. Furche, N. Morgner, O. Kostko, B. V. Issendorff, and M. M. Kappes, *Angew. Chem., Int. Ed.* **46**, 2944 (2007).
- ⁴⁵N. Shao, W. Huang, Y. Gao, L. M. Wang, X. Li, L. S. Wang, and X. C. Zeng, *J. Am. Chem. Soc.* **132**, 6596 (2010).
- ⁴⁶N. Shao, W. Huang, W. N. Mei, L. S. Wang, Q. Wu, and X. C. Zeng, *J. Phys. Chem. C* **118**, 6887 (2014).
- ⁴⁷W. Huang, M. Ji, C. D. Dong, X. Gu, L. M. Wang, X. G. Gong, and L. S. Wang, *ACS Nano* **2**, 897–904 (2008).
- ⁴⁸S. Pande, W. Huang, N. Shao, L. M. Wang, N. Khetrapal, W. N. Mei, T. Jian, L. S. Wang, and X. C. Zeng, *ACS Nano* **10**, 10013 (2016).
- ⁴⁹D. J. Wells and R. S. Berry, *Phys. Rev. Lett.* **73**, 2875 (1994).
- ⁵⁰D. J. Wales and J. P. K. Doye, *J. Chem. Phys.* **103**, 3061–3070 (1995).
- ⁵¹M. Schmidt, R. Kusche, T. Hippler, J. Donges, W. Kronmller, B. V. Issendorff, and H. Haberland, *Phys. Rev. Lett.* **86**, 1191 (2001).
- ⁵²F. Calvo, *Phys. Chem. Chem. Phys.* **17**, 27922 (2015).
- ⁵³Z. H. Li and D. G. Truhlar, *Chem. Sci.* **5**, 2605 (2014).
- ⁵⁴A. Aguado and M. F. Jarrold, *Annu. Rev. Phys. Chem.* **62**, 151 (2011).
- ⁵⁵Z. H. Li, A. W. Jasper, and D. G. Truhlar, *J. Am. Chem. Soc.* **129**, 14899 (2007).
- ⁵⁶F. Zaera, *Chem. Rev.* **112**, 2920 (2012).
- ⁵⁷M. Losurdo, A. Suvorova, S. Rubanov, K. Hingerl, and A. S. Brown, *Nat. Mater.* **15**, 995 (2016).
- ⁵⁸Y. Engelmann, A. Bogaerts, and E. C. Neyts, *Nanoscale* **6**, 11981 (2014).
- ⁵⁹Y. Gao, N. Shao, Y. Pei, Z. Chen, and X. C. Zeng, *ACS Nano* **5**, 7818 (2011).
- ⁶⁰J. B. Witkoski and D. J. Doren, *J. Chem. Theory Comput.* **1**, 14 (2005).
- ⁶¹T. B. Blank and S. D. Brown, *J. Chemom.* **8**, 391 (1994).
- ⁶²S. S. Haykin, *Kalman Filtering and Neural Networks* (John Wiley & Sons Inc., New York, USA, 2001), Vol. 304.
- ⁶³G. Kresse and J. Hafner, *Phys. Rev. B* **47**, 558 (1993); G. Kresse and J. Furthmller, *ibid.* **54**, 11169 (1996); G. Kresse and J. Hafner, *J. Phys.: Condens. Matter* **6**, 8245 (1994).
- ⁶⁴J. P. Perdew, K. Burke, and M. Ernzerhof, *Phys. Rev. Lett.* **77**, 3865 (1996).
- ⁶⁵G. Kresse and D. Joubert, *Phys. Rev. B* **59**, 1758 (1999).
- ⁶⁶R. P. Gupta, *Phys. Rev. B* **23**, 6265 (1981).
- ⁶⁷A. Bruma, R. Ismail, N. L. Oliver Paz-Borbo, H. Arslan, G. Barcaro, A. Fortunelli, Z. Y. Li, and R. L. Johnston, *Nanoscale* **5**, 646 (2013).
- ⁶⁸D. J. Wales and H. A. Scheraga, *Science* **285**, 1368 (1999).
- ⁶⁹S. Bulusu and X. C. Zeng, *J. Chem. Phys.* **125**, 154303 (2006).
- ⁷⁰B. Assadollahzadeh and P. Schwerdtfeger, *J. Chem. Phys.* **131**, 064306 (2009).
- ⁷¹L. Yan, L. Cheng, and J. Yan, *J. Phys. Chem. C* **119**, 23274–23278 (2015).
- ⁷²C. D. Dong and X. G. Gong, *J. Chem. Phys.* **132**, 104301 (2010).
- ⁷³P. Labastie and R. L. Whetten, *Phys. Rev. Lett.* **65**, 1567 (1990).
- ⁷⁴R. Poteau, F. Spiegelmann, and P. Labastie, *Z. Phys. D: At., Mol. Clusters* **30**, 57 (1994).

- ⁷⁵F. Calvo and P. Labastie, *Chem. Phys. Lett.* **247**, 395 (1995).
- ⁷⁶M. Eryurek and M. H. Guven, *Phys. A* **377**, 514 (2007).
- ⁷⁷P. Chandrachud, K. Joshi, S. Krishnamurthy, and D. G. Kanhere, *J. Phys.* **5**, 72 (2009).
- ⁷⁸H. Hakkinen, M. Walter, and H. Gronbeck, *J. Phys. Chem. B* **110**, 9927 (2006).
- ⁷⁹M. Walter, J. Akola, O. Lopez-Acevedo, P. D. Jazdzinsky, G. Calero, C. J. Ackerson, R. L. Whetten, H. Gronbeck, and H. Hakkinen, *Proc. Natl. Acad. Sci. U. S. A.* **105**, 9157 (2008).
- ⁸⁰J. Akola, M. Walter, R. L. Whetten, H. Hakkinen, and H. Gronbeck, *J. Am. Chem. Soc.* **130**, 3756 (2008).
- ⁸¹A. Aguado and J. M. Lopez, *J. Phys. Chem. Lett.* **4**, 2397 (2013).
- ⁸²A. Aguado, *J. Phys. Chem. C* **115**, 13180 (2011).
- ⁸³M. A. Carignano and I. Gladich, *Europhys. Lett.* **90**, 63001 (2010).
- ⁸⁴J. A. Reyes-Nava, I. L. Garzon, and K. Michaelian, *Phys. Rev. B* **67**, 165401 (2003).
- ⁸⁵L. Brewer, Report 3720, Lawrence Berkeley Laboratory, Berkeley, CA, 1973.
- ⁸⁶T. L. Hill, *An Introduction to Statistical Thermodynamics* (Addison-Wesley, Reading, MA, 1960), p. 149.
- ⁸⁷D. A. McQuarrie, *Statistical Mechanics* (Harper & Row, New York, 1975), p. 130.